

MEASURING THE SOLAR RADIUS FROM SPACE DURING THE 2012 VENUS TRANSIT

M. EMILIO^{1,2}, S. COUVIDAT³, R. I. BUSH³, J. R. KUHN², AND I. F. SCHOLL²

¹ Observatório Astronômico Departamento de Geociências, Universidade Estadual de Ponta Grossa, Paraná, Brazil; memilio@uepg.br

² Institute for Astronomy, University of Hawaii, Honolulu, HI 96822, USA; kuhn@ifa.hawaii.edu, ifscholl@hawaii.edu

³ HEPL Solar Physics, Stanford University, Stanford, CA 94305, USA; couvidat@stanford.edu, ribush@solar.stanford.edu

Received 2014 July 3; accepted 2014 October 7; published 2014 December 18

ABSTRACT

We report in this work the determination of the solar radius from observations by the Helioseismic and Magnetic Imager (HMI) and the Atmospheric Imaging Assembly (AIA) instruments on board the *Solar Dynamics Observatory* during the 2012 June Venus transit of the Sun. Two different methods were utilized to determine the solar radius using images of Sun taken by the HMI instrument. The first technique fit the measured trajectory of Venus in front of the Sun for seven wavelengths across the Fe I absorption line at 6173 Å. The solar radius determined from this method varies with the measurement wavelength, reflecting the variation in the height of line formation. The second method measured the area of the Sun obscured by Venus to determine the transit duration from which the solar radius was derived. This analysis focused on measurements taken in the continuum wing of the line, and applied a correction for the instrumental point spread function (PSF) of the HMI images. Measurements taken in the continuum wing of the 6173 Å line, resulted in a derived solar radius at 1 AU of $959''.57 \pm 0''.02$ ($695,946 \pm 15$ km). The AIA instrument observed the Venus transit at ultraviolet wavelengths. Using the solar disk obscuration technique, similar to that applied to the HMI images, analysis of the AIA data resulted in values of $R_{\odot} = 963''.04 \pm 0''.03$ at 1600 Å and $R_{\odot} = 961''.76 \pm 0''.03$ at 1700 Å.

Key words: astrometry – Sun: fundamental parameters – Sun: photosphere

1. INTRODUCTION

Since the beginning of the 18th century, independent determination of the astronomical unit allowed planetary transits to be used to measure the solar radius (Parkinson et al. 1980; Shapiro 1980). Similarly, the solar diameter has been determined from precise measurements of total solar eclipses (Sofia et al. 1983; Kubo 1993; Kilcik et al. 2009).

The true solar radius is still a matter of debate in the literature as differences of several tenths of an arcsecond (i.e., about 500 km) are observed between various groups. Indeed, modern values cited for the solar radius range from $958''.54 \pm 0''.12$ (Sánchez et al. 1995) to $960''.62 \pm 0''.02$ (Wittmann 2003) (for a review, see Kuhn et al. 2004; Emilio & Leister 2005; Thuillier et al. 2005; Rozelot & Damiani 2012; Emilio et al. 2012). This range is mainly due to systematic errors from different instruments and observers, since the uncertainties claimed in each paper and for a specific instrument are typically an order of magnitude smaller than the difference between groups. Evidently the uncertainties reported reflect statistical errors from averaging many measurements by single instruments and not systematic errors between measurement techniques.

Because measurements from space of Mercury and Venus transits of the Sun are not affected by optical distortions caused by the Earth’s atmosphere, they have significant advantages over ground observations. The stellar photosphere is defined as the layer from which its visible light originates (~ 5000 Å), that is, where the optical depth is two-thirds in the star’s continuum, since this is the average level in the atmosphere from which photons escape. In this work, the solar limb was determined adopting the inflection point of the limb darkening function (LDF) as a reference. This is a common definition of the solar limb adopted in many works.

The first measurement of solar radius from space using the planetary timing technique is reported in Emilio et al. (2012). The value found was $960''.12 \pm 0''.09$ ($696,342 \pm 65$ km)

determined from the 2003 and 2006 Mercury transits of the Sun using the Michelson Doppler Imager (MDI) on board the *Solar and Heliospheric Observatory* (SOHO). More recently, Meftah et al. (2014b) and Hauchecorne et al. (2014) reported a measurement of solar radius during the Venus transit of $959''.85 \pm 0''.19$ for SODISM/PICARD at 6071 Å. The work by Hauchecorne et al. (2014) also determined a solar radius of $959''.90 \pm 0''.06$ using HMI/SDO images at 6173 Å during the Venus transit.

The solar radius values determined by Hauchecorne et al. (2014) are not comparable with Emilio et al. (2012) radius because the authors adopted a definition of solar radius that is not based on the inflection point of the solar LDF. The Hauchecorne et al. (2014) analysis determined the Venus contact times based on the decrease in solar radiance in a region around the contact positions between Venus and the Sun in order to find the solar radius at the “base” of the LDF. Because it is unclear where in the LDF the solar radius is defined with this technique, this makes the comparison with our results and previous measurements in the literature difficult.

This work details the solar radius determined during the Venus transit of 2012 June by the Helioseismic and Magnetic Imager (HMI) and the Atmospheric Imaging Assembly (AIA) instruments on the *Solar Dynamics Observatory* (SDO) spacecraft. The HMI observations taken during the Venus transit are described in Section 2.

Section 3 describes the solar radius determined by fitting the Venus trajectory in front of the Sun using HMI images taken across the Fe I 6173.34 Å absorption line. The solar radius using this method has been determined for six wavelengths across the Fe line in left circular polarization (LCP) and right circular polarization (RCP) and in the continuum wing at four linear polarizations.

In Section 4, a second method to determine the solar radius utilizes the obscuration of the solar disk by Venus as it passes the solar limb. In addition, this method compares the solar

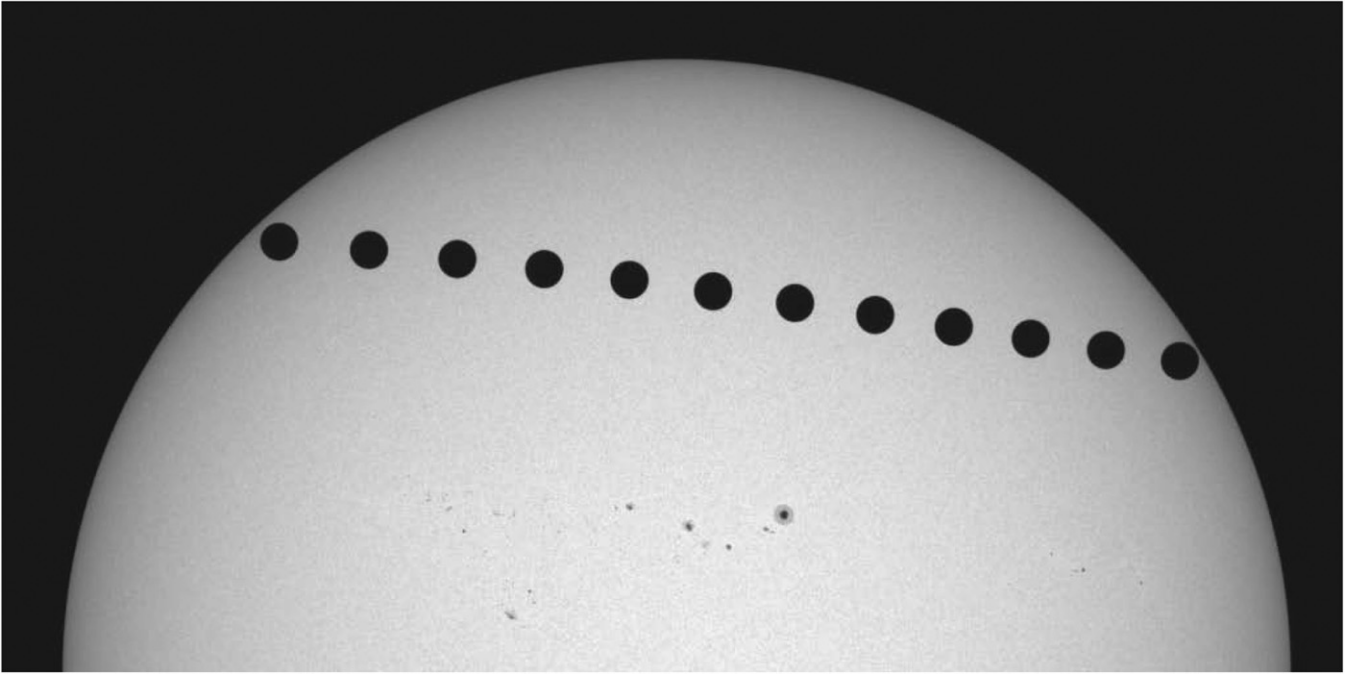


Figure 1. This composite image shows the Sun during the Venus transit as observed by the HMI instrument. This image consists of vertical segments of continuum tuned images containing the Venus silhouette taken every 31.25 minutes with the HMI side camera.

radius obtained from HMI images with and without point spread function (PSF) correction. Both methods in Sections 3 and 4 use the distance between the solar center and inflection point at the LDF as a definition for the solar radius.

The AIA observations taken during the Venus transit are described in Section 5. In Section 6, we present results of the solar radius determination using AIA images taken at 1600 Å and 1700 Å. Section 7 summarizes the paper and discusses our results.

2. HMI OBSERVATIONS DURING THE VENUS TRANSIT

The HMI instrument on the *SDO* spacecraft observed the Venus transit of the Sun on 2012 June 5–6. During the transit, HMI obtained full disk images in wavelength in and adjacent to the Fe I 6173.34 Å solar absorption line using two CCD cameras with 4096×4096 pixel resolutions. Both HMI cameras operated with an image cadence of 3.75 s with the exposures alternating between the two cameras.

The standard HMI observing sequence was modified during the Venus transit by replacing images normally taken by the HMI side camera for the vector magnetic field observations with images taken at four linear polarizations in the continuum at the wing of the Fe absorption line. In terms of Stokes parameters, the side camera observing sequence was $I+Q$, $I-Q$, $I+U$, and $I-U$ (linear polarizations at 0, 90, 45, and 135 deg with respect to solar north). The standard line-of-sight velocity and magnetic field observing sequence was continued on the front HMI camera with images taken in LCP and RCP at six wavelengths across the Fe line. The initial processing of the HMI raw images to level 1 data had overscan rows and columns removed, the dark frame and CCD bias subtracted, and a gain correction applied to generate a uniform series of flat fielded images. Figure 1 shows a composite image of the Sun during the Venus as observed by the HMI instrument. This image consists of vertical segments of continuum tuned images containing the Venus silhouette

taken every 31.25 minutes (every 500th image) with the HMI side camera.

The *SDO* ephemeris was computed by the NASA Goddard Space Flight Center Flight Dynamics Group and provides the location of the Venus center with respect to the Sun center as observed at the *SDO* location with one second cadence time resolution. Using the ephemeris values of the Sun–*SDO* distance during the transit, the total duration of the Venus transit across the Sun is then converted to an equivalent solar radius and corrected to a reference distance of 1 AU. A final small adjustment on the order of 0'.01 is applied to correct for the finite Sun–*SDO* distance. The apparent diameter is affected by the Sun to spacecraft distance; the Sun appears slightly larger than geometric radius because the tangent to the observed limb is not parallel to the line from the spacecraft to the sub-solar point.

3. SOLAR RADIUS DETERMINED FROM THE TRAJECTORY OF THE VENUS TRANSIT

The observed solar LDF is a result of the convolution of the true solar LDF with the instrumental PSF. The Earth's atmosphere, in the case of ground observations, and instrumental imperfections may result in the observed LDF varying around the solar circumference. Because measurement uncertainty may be due to systematic errors in the instrument, observations, or the analysis techniques, additional individual observations may not improve the absolute accuracy of the solar radius measurement. In order to address this issue, the current analysis fits the entire trajectory of Venus across the Sun in order to determine when the center of Venus crossed the solar limb. The same fit along the complete six hour transit event was used to find the geometric positions at ingress and egress.

A total of 16 sets of HMI images with different wavelengths and polarization states were processed to determine the solar radius. The side camera obtained images with a single wavelength

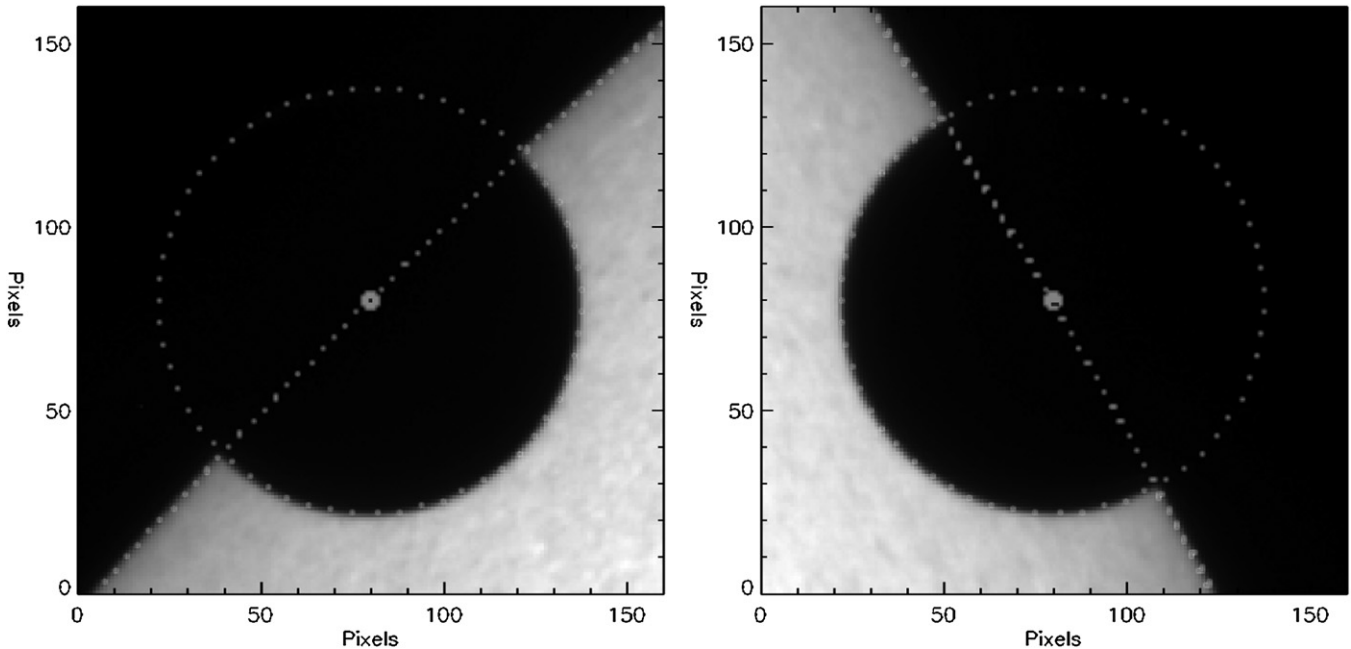


Figure 2. Portion of the HMI continuum tuned images taken near the contact times for the Venus ingress (left) and egression (right). The dashed lines show the fits to the Venus and solar limbs as well as the Venus center location.

in four linear polarizations and the front camera observed at six wavelengths across the Fe I line in two circular polarizations (LCP and RCP). In total, about 6000 images were analyzed during the transit.

Figure 2 shows images of the Sun containing Venus at the time when the center of Venus passes the solar limb for both ingress and egress. The contact times vary as a function of the observing wavelength, but there is no significant dependence on the observed polarization state.

The trajectory fitting procedure follows that described in (Emilio et al. 2012). For each image with a specific wavelength and polarization configuration, a previous image of the Sun taken with the same instrument setting but without Venus was subtracted. This minimized the effects of the limb darkening gradient and provided a more accurate determination of the center of Venus on the solar disk. The apparent edge of Venus was fit to an ellipse with the center of the ellipse adopted as the center of Venus. All HMI images taken between the first and fourth contacts of Venus with the Sun were processed to determine the location of the center of Venus on the solar disk. Approximately 0.6% of the total number of available images were discarded from further analysis because the center-determination errors were large when Venus was close to the solar limb.

The positions of the center of the Sun and the limb were calculated as described in Emilio et al. (2000). A polynomial was fit to the x - y pixel coordinates of Venus's center during the image timeseries. This transit trajectory was extrapolated to find the precise geometric intersection with the limb by also iteratively accounting for the apparent change in the solar radius. The contact times were found from a least-squares fit of Venus's center position trajectory $x(t)$ and $y(t)$ to the intersection with the limb near first/second and third/fourth contact for each instrumental configuration using a sixth-order polynomial function. Figure 3 illustrates the trajectory of Venus across the solar disk and the difference between the x and y positions of the center of Venus compared to the sixth-order polynomial fit.

Finally, from these two contact times the total duration of the Venus transit as seen from HMI is derived. The extrapolated times of the Venus center crossing of the solar limb, the transit duration and the corresponding solar radius are provided in Table 1. The same procedure was performed independently for each wavelength and polarization timeseries.

A very clear wavelength dependence of the inferred solar radius across the Fe I 6173 Å line is shown in Figure 4. The difference in the solar radius near the line core compared to the continuum wing is 0'.23 corresponding to a radius difference of about 167 km, which is significantly larger than the estimated error in the measurements. As expected, the line core shows a larger radius meaning those photons, on average, came from a region higher in the solar atmosphere. Norton et al. (2006) discusses the Fe I 6173 Å and estimates that the line core height of formation is approximately 250–290 km above the line continuum height of formation. Our measured radius difference between the line core and line continuum is smaller than those discussed in Norton et al. (2006) because the HMI instrument is sampling over a range of wavelengths and the spacecraft motion relative to the Sun also shifts the sampling position in the line.

The measured transit time and the derived solar radius show no significant differences for the four linear polarizations at the continuum tuning wavelength (-0.342 mÅ). The LCP/RCP polarization measurements across the line vary ± 0.01 mÅ for each tuning wavelength, but there is no meaningful dependence with polarization. The accuracy of the LCP/RCP measurements is slightly less than for the linear polarization measurements because there were one-third fewer images for the circular polarization measurements than for the linear polarization measurements.

During the transit of Venus across the solar disk, the planet travels from the east to the west limb. Combined with the change in orbital velocity of *SDO* during the same time interval, this results in a significant change in the average Doppler velocity at the solar surface around Venus. At 22:20 UT on 2012 June 5 (ingression), the average solar Doppler velocity near Venus is

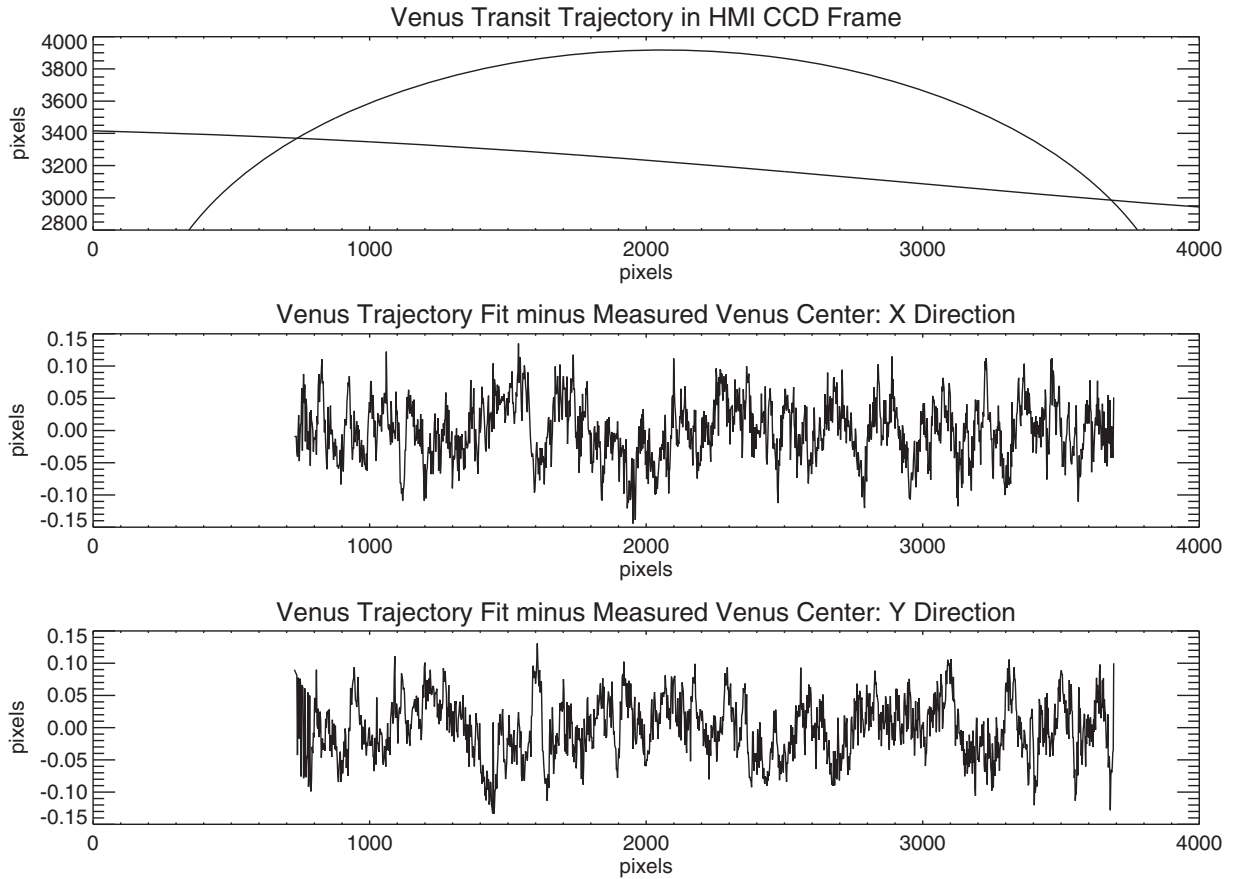


Figure 3. Top panel shows the Venus trajectory in the HMI detector frame. The middle and bottom panels, respectively, plot the residuals of the Venus trajectory in the X and Y HMI detector frame after subtracting a sixth-order polynomial fit.

Table 1
2012 Venus Transit Results

ID ^a	Wavelength ^b	Polarization	Ingress ^c	Egress ^c	Duration ^d	Radius ^e
10004	-342	I+Q; 0 lin	136.9595	505.0547	368.0952	959.62
10005	-342	I-Q; 90 lin	136.9601	505.0551	368.0950	959.62
10006	-342	I+U; 45 lin	136.9600	505.0573	368.0973	959.62
10007	-342	I-U; 135 lin	136.9587	505.0530	368.0943	959.62
10058	-172	I+V; LCP	136.9615	505.0633	368.1018	959.63
10059	-172	I-V; RCP	136.9658	505.0641	368.0983	959.63
10078	-103	I+V; LCP	136.9568	505.0614	368.1046	959.64
10079	-103	I-V; RCP	136.9587	505.0591	368.1004	959.63
10098	-34	I+V; LCP	136.9309	505.0760	368.1451	959.70
10099	-34	I-V; RCP	136.9255	505.0793	368.1538	959.71
10118	+34	I+V; LCP	136.8901	505.1337	368.2437	959.85
10119	+34	I-V; RCP	136.8957	505.1328	368.2371	959.84
10138	+103	I+V; LCP	136.9318	505.1281	368.1963	959.78
10139	+103	I-V; RCP	136.9334	505.1259	368.1925	959.77
10158	+172	I+V; LCP	136.9621	505.0710	368.1088	959.64
10159	+172	I-V; RCP	136.9629	505.0747	368.1118	959.65

Notes.

^a Filtergram identification number.

^b Displacement in mÅ from core of Fe I line at 6173.34 Å.

^c Time in minutes from 2012 June 5 20:00 UTC.

^d Time in minutes between Venus center limb crossing.

^e Solar radius in arcseconds at 1 AU.

about 670 m s^{-1} , while at 4:25 UT on the next day (egression) this velocity reaches 2900 m s^{-1} . In other words, the Fe I line profile has been shifted by 2230 m s^{-1} from ingress to egression, which corresponds to a Doppler shift of about 46 mÅ .

Therefore, any result of solar radius measurements obtained at a specific wavelength with HMI comes with the caveat that the solar line has slightly shifted during the measurement. This is illustrated in the lower panel of Figure 4, which shows the

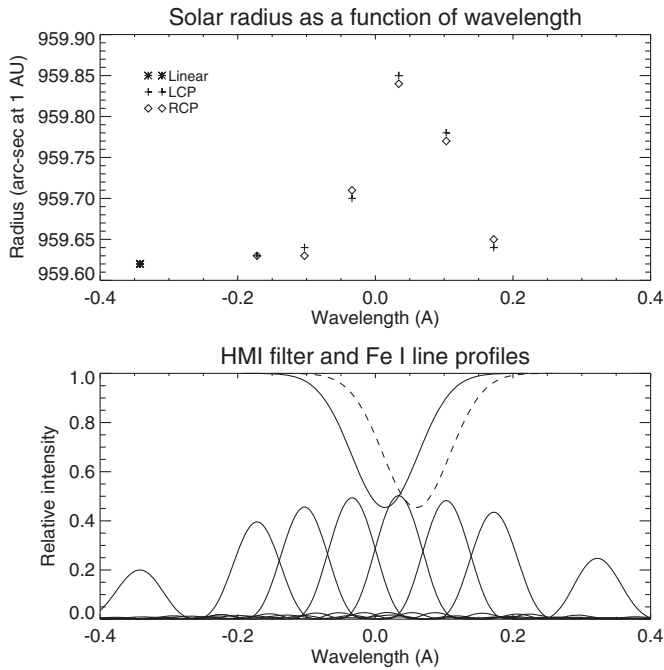


Figure 4. Top panel shows the solar radius determined from the HMI images of the Venus transit as a function of wavelength across the Fe I line and for different polarization states. There is a significant variation of the solar radius as a function of the observing wavelength, but there is no meaningful dependence on polarization. The lower curves in the bottom panel show the HMI filter profiles relative to the Fe absorption line at ingress (upper solid line) and egress (upper dashed line).

typical HMI filter-transmission profiles and a model of the Fe I line shifted with respect to these profiles from ingress to egress. Consequently, a definitive measurement of the height of formation of the line in the solar atmosphere is not possible, but the measurements give a reasonable estimate of the variation.

A comparison of the results of polynomial fits to the Venus trajectory for the linear polarization measurement provides an estimate of the accuracy of the solar radius determination. Table 2 shows the derived solar radius for the four linear polarization measurements for polynomial fits to the measured trajectory, for fit degrees from 4 to 7. There is a systematic variation of the derived radius as a function of the fit degree, and the standard deviation for the measurements for fit degrees of 4, 5 and 6 are consistent. The mean and standard deviation of these fits is consequently $959'63 \pm 0'02$. The error estimates are a combination of the statistical errors of the different polarization measurements and the systematic errors of the fitting techniques.

4. SOLAR RADIUS DETERMINED BY VENUS OBSCURATION OF THE SOLAR DISK

This method infers the solar radius from the duration of the transit based on the time the center of Venus crosses the solar limb at ingress and egress. The center of Venus is deemed to cross the solar limb when the measured surface area of the planet's shadow inside the solar disk is equal to 0.4946 times its maximum surface area.

Here, this corrective factor is determined in two different ways. First, a value is calculated based on the analytical formula of circle-circle intersection. Second, a code is used to simulate this intersection and to derive its surface area (using actual sizes of the Sun and Venus in HMI pixels). Both analytical and simulated results are slightly different due to the finite size of the

Table 2
Comparison of HMI Polynomial Fits

Degree	10004	10005	10006	10007	Mean	Std. Dev.
4	959.647	959.644	959.649	959.643	959.646	0.0027
5	959.638	959.636	959.641	959.634	959.637	0.0027
6	959.621	959.621	959.624	959.620	959.621	0.0020
7	959.600	959.612	959.629	959.629	959.617	0.0140

HMI pixels: with actual HMI images, a pixel is either entirely inside or entirely outside the solar disk (therefore, the surface area of Venus inside the solar disk varies by integer units of pixel area). This difference between simulated and analytical values is a small source of error in our estimate of the solar radius.

Only HMI images from the side camera were used because they were taken at the same wavelength and provided a consistent reference solar limb. Similarly, all four linear polarizations were used in the analysis because, as discussed in the previous section, there was no discernible variation in the limb profile as a function of the polarization. This set of images provided a 3.75 s resolution of the ingress and egress. A total of 816 images were used in the analysis: 2012.06.05_22:03:00 TAI to 2012.06.05_22:27:00 TAI during ingress and 2012.06.06_04:14:00 TAI to 2012.06.06_04:41:00 TAI during egress.

The flat-fielded images were processed to remove the instrumental distortion using estimates obtained from ground-calibration data (Wachter et al. 2012). A PSF correction was performed using a Richardson-Lucy algorithm applied to the entire images, with 25 iterations, with the PSF assumed to be constant across the HMI CCDs and with no azimuthal dependence. An estimate of the PSF obtained from Venus-transit data is used (A. Norton 2013, private communication), rather than the initial estimate obtained from ground data and published in Wachter et al. (2012). The method presented in this section to estimate the solar radius is sensitive to the HMI PSF and in the way this PSF is corrected.

The limb finder implemented in the HMI production pipeline was run to locate the center position of the solar disk and to estimate the radius in pixels at each time step, defined as the inflection point of the LDF. Figure 5 shows this LDF and its derivative for a typical HMI image before and after the PSF has been removed. The vertical line shows the location of the inflection point as determined by the limb finder.

By averaging 80 images prior to first contact with Venus, and separately averaging 80 images after last contact, two background images of the Sun were produced. Each of the 816 images was then divided by the appropriate background image. For each image, a mask based on the limb finder image center position and limb radius was created: the pixels inside the solar disk were set to one, while those outside were set to zero. Each image was then multiplied by its mask. The last step in image processing is to set a threshold and to assign each pixel inside the solar disk (mask is non-zero) and whose intensity is below this given threshold to the Venus disk. By counting the total number of pixels satisfying this criterion, a measurement of the surface area of Venus inside the solar disk is obtained as a function of time, separately for ingress and egress (Figure 6). A third-order polynomial fit of this surface area as a function of time is used to determine the precise times of contact.

From the *SDO* ephemeris, the total duration of the Venus transit is computed as a function of the solar radius. Deriving the solar radius R_{\odot} seen from HMI simply requires interpolating

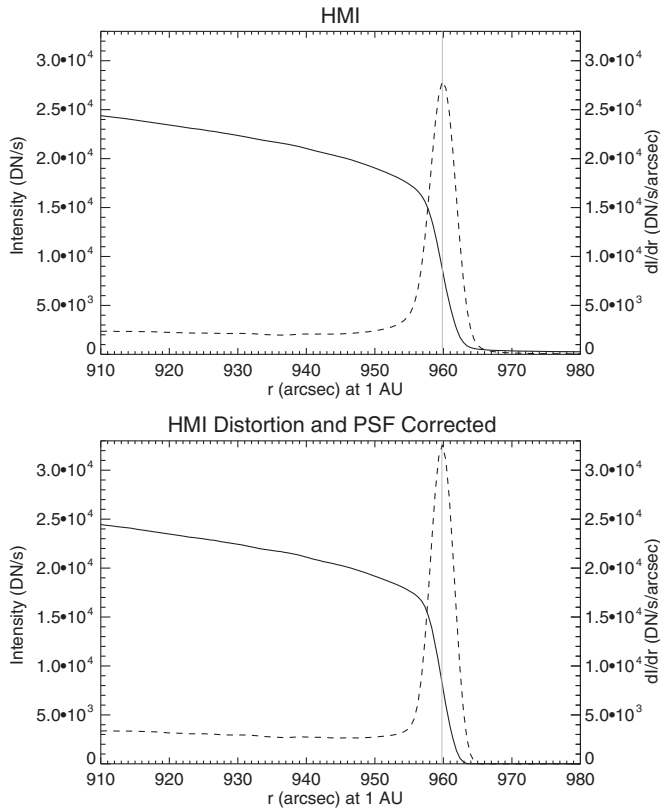


Figure 5. Limb darkening functions (solid lines) and derivatives of these functions (dashed lines) are plotted for an HMI image before (upper panel) and after (lower panel) correcting for the instrumental PSF and distortion. The vertical lines show the location of the maximum of the derivative of the limb darkening function.

the ephemeris durations at the measured duration, using a linear fit. Here the best estimate derived is $R_{\odot} = 959'58$ at 1 AU, corresponding to a total transit time for Venus of 6 hr 8 minutes and 4.72 s. In addition to an adjustment of the measured radius to a constant Sun to spacecraft distance of 1 AU, a decrease of $0'01$ is needed to correct for the finite distance to the Sun. This gives a final value of the solar radius at 6173 \AA of $959'57 \pm 0'02$ ($695,946 \pm 15 \text{ km}$) at 1 AU. Here, we use the same error estimate as the one derived in the previous section; again, this is a combination of systematic and statistical uncertainty.

The radius obtained in this section is consistent with the one discussed earlier using the trajectory of the Venus transit, which does not include the image deconvolution by the PSF. Indeed, removing the PSF from level 1 images lowers the solar radius by about $0'07$ at 1 AU. Similarly, once this impact of the PSF is considered, our result is also close to the radius determined on level 1 images by the limb finder and the HMI plate scale (both stored as keywords in the level 1 records): the plate scale was estimated independently from Venus transit data (J. Schou 2012, private communication). Therefore, these three independent methods return values in close agreement.

5. AIA OBSERVATIONS

Of interest are the images at 1600 \AA and 1700 \AA that are formed at average heights of, respectively, 430 and 360 km above the photospheric continuum (Fossum & Carlsson 2005) but whose sensitivity functions cover a wide range of heights. Indeed, these images show significant sensitivity to the

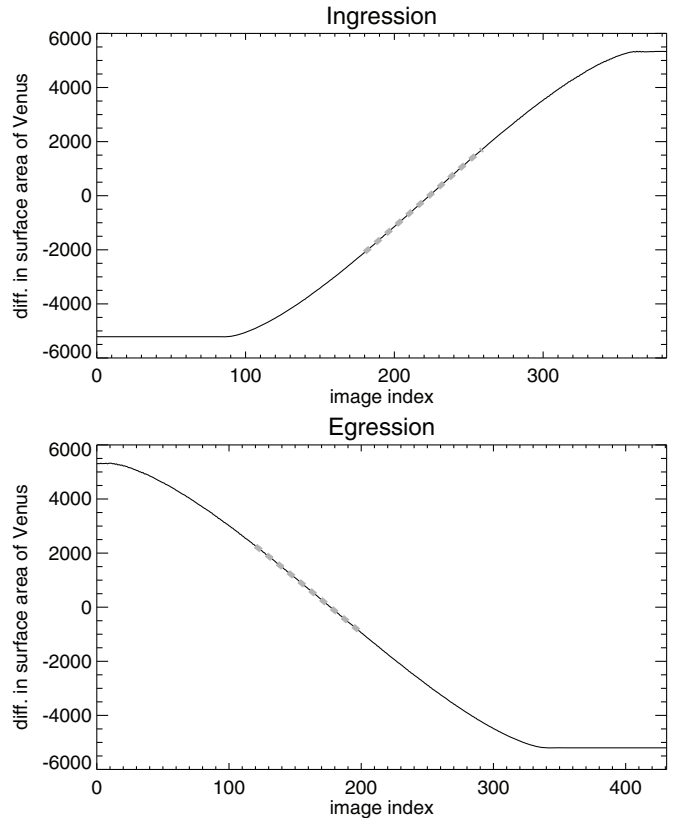


Figure 6. These plots show the area (in pixels) of Venus covering the solar disk minus the expected area at the time of contact between the center of Venus and the solar limb during ingress (top) and egression (bottom). The thick dashed portion of the lines indicates the third-order polynomial fit of this curve that is used to precisely determine the contact times at ingress and egression.

chromosphere and the transition region, as the presence of chromospheric network attests.

During the Venus transit, the AIA instrument ran a modified observing program in order to obtain higher cadence EUV images; however, the 1600 and 1700 images were both taken with a 24 s cadence rather than the 3.75 s of the HMI images. In order to use lossless compression for the Venus transit images, only the top 68% of the image was downlinked. A full disk 1700 image was taken every 96 s, but the full disk 1600 images were available only before and after the transit.

A limb finder is not routinely run on AIA images because changing conditions in the solar chromosphere and corona make limb determination difficult. In order to determine the solar limb in the AIA images, however, a modified version of the HMI-pipeline limb finder was run on AIA data. Like with HMI, this limb finder computes the derivative of the LDF and locates the maximum of this derivative. To improve image cadence, partial AIA images containing only the Venus transit path were sent to the ground. Therefore, the limb finder was only run on AIA data prior to, and after, the transit. Instrumental distortion and PSF were not removed from the AIA images because they have not been precisely determined for AIA.

6. SOLAR RADIUS DETERMINATION AT 1600 AND 1700 \AA

Similar to the solar disk obscuration technique used for HMI, the solar radius at 1600 and 1700 \AA were determined from the AIA observations. The image processing applied to AIA data is similar to the one described for the HMI analysis except without

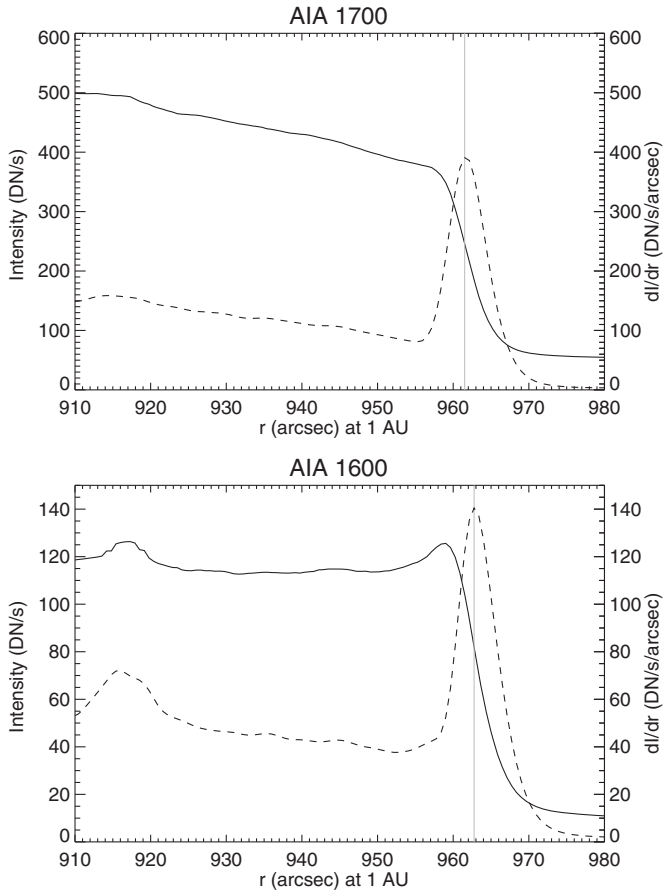


Figure 7. Limb darkening functions (solid lines) and derivatives of these functions (dashed lines) are plotted for an AIA 1700 Å image (upper panel) and an AIA 1600 Å image (lower panel). The vertical lines show the location of the maximum of the derivative of the limb darkening function.

the distortion and PSF image corrections. The solar radius was then determined from the times that the Venus center crossed the solar limb in conjunction with the ephemeris provided by the Goddard Space Flight Center.

For AIA 1600 Å and prior to the Venus ingress, the average radius difference between the limb-finder results and a reference solar radius is 4.7 pixels, while for AIA 1700 Å it is 2.75 pixels. This large discrepancy most likely results from the sensitivity of the two AIA channels to chromospheric and transition-region signal. Figure 7 shows typical limb darkening profiles for AIA images in the two UV channels. These LDFs differ significantly from the that of the HMI (see Figure 5). In particular, for AIA 1600 Å there is an increase in intensity right at the limb.

The following R_{\odot} estimates at 1 AU are obtained: $R_{\odot} = 963''.04$ at 1600 Å and $R_{\odot} = 961''.76$ at 1700 Å, corresponding to total transit durations of 6 hr 10 minutes 16.8 s and 6 hr 9 minutes 27.89 s, respectively.

Limitations in the data processing (instrumental distortion and PSF not removed, temporal cadence coarser than for HMI, etc.) make the uncertainty of these results larger than those based on HMI data. Some estimates for the error bars on the AIA results can be determined from the FWHM of the derivative of the LDF (in arcseconds at 1 AU): for HMI without distortion and PSF corrections: $4''.55$; for HMI with distortion and PSF corrections: $4''.14$; for AIA 1700: $6''.27$; for AIA 1600: $6''.53$. Therefore, multiplying the error estimates determined for HMI in this paper by the ratio of the AIA to HMI FWHM of the

Table 3
Comparison of AIA Polynomial Fits

Wavelength	Degree 1	Degree 2	Degree 3	Mean	Std. Dev.
1600	963.094	963.070	963.040	963.068	0.027
1700	961.739	961.775	961.762	961.759	0.018

derivative of the LDF result in error estimates of $0''.03$ for AIA 1600 and 1700 radius determination.

Table 3 gives the estimated solar radius as a function of the degree of the polynomial fit of the surface area of Venus inside the solar disk. For both AIA 1600 and 1700 determinations, the range of the radius determined by different polynomial fits is similar to the error based on the derivation of the limb profile FWHM.

7. DISCUSSION AND CONCLUSIONS

Two different methods have been used to determine the solar radius. One is based on the Venus trajectory across the solar disk and utilizes images uncorrected for the HMI PSF, while the other is based on the obscuration of the solar disk and utilizes images corrected for this PSF. The initial radii determined by these two methods differ by $0''.06$, which is compatible with the PSF correction. Indeed, deconvolving HMI images by the PSF lowers their radius by $0''.07$. Therefore, the difference in radii values between the methods is consistent with the estimate of the PSF correction. Consequently, we provide only one solar radius value as our final result. This value takes the PSF impact into account and is accompanied by an error bar that includes both the statistical and systematic errors (excluding the PSF correction).

Measurements taken in the continuum wing of the 6173 Å line, result in a solar radius determination at 1 AU of $959''.57 \pm 0''.02$ ($695,946 \pm 15$ km). The difference in the solar radius determined from measurements near the line core and in the continuum wing is $0''.23$ corresponding to a radius difference of about 167 km. This radius difference is consistent with the difference in the height of formation of the line core to the line wing, and is significantly larger than the estimated error in the radius measurements. For AIA, we found the values $R_{\odot} = 963''.04 \pm 0''.03$ at 1600 Å and $R_{\odot} = 961''.76 \pm 0''.03$ at 1700 Å. Because there are additional systematic uncertainties that are either not known or have not been completely included, the above measurement uncertainties have likely been underestimated.

The value of the solar radius described in this paper is not consistent with the previous values found with MDI Mercury transits and further work will be done to check both the optical model and the ephemerides. Even though the continuum values found here are not affected by those systematics, they still differ significantly from the results from the Mercury transit of 2003 and 2006 as seen from MDI-SOHO (Emilio et al. 2012). Because the solar radius determinations from the MDI observations of the 2003 and 2006 Mercury transits agree with each other, it is difficult to identify a basis for the difference with the HMI measurements. The MDI instrument has an astigmatism that made the inflection point definition different from ingress and egress on Mercury transit. The PSF of MDI is a very complicated one and changes around the limb, affecting the solar LDF. This can add a systematic error that can affect both 2003 and 2006 solar radii determinations by MDI-SOHO during the Mercury transit.

From Table 3 of Sofia et al. (2013), the average value of the solar radius measured by the Solar Disk Sextant instrument during balloon flights from 1992 to 2011 is $959'76 \pm 0'12$ at 6150 \AA . Meftah et al. (2014a) recently reported solar radius values made by the ground based SODISM II instrument of $959'78 \pm 0'19$ at 5358 \AA and $959'86 \pm 0'18$ at 6071 \AA . These measurements are within 2σ of the HMI solar radius determination at 6173 \AA ; however, the measurement uncertainties mask any details of the radius variation as a function of wavelength.

We thank A. Norton and T. Duvall for the HMI PSF determination and I. Cunnyngham and J. Sommers for assistance in processing the HMI and AIA data.

This research was supported by the NASA program through a grant to the IfA, by the NASA grant 12-SHP 12/2-0080 and the NASA Helioseismic and Magnetic Imager contract NAS5-02139 to Stanford and subcontract to the IfA. This work was also partially supported by CNPq grants 312738/2013-7 and 480029/2011-3, Fundação Araucária convênio 228/2014 and the Instituto Nacional de Estudos do Espaço (CNPq), and NASA grant NNX13AE08G.

REFERENCES

- Emilio, M., Kuhn, J. R., Bush, R. I., & Scherrer, P. H. 2000, *ApJ*, **543**, 1007
- Emilio, M., Kuhn, J. R., Bush, R. I., & Scholl, I. F. 2012, *ApJ*, **750**, 135
- Emilio, M., & Leister, N. V. 2005, *MNRAS*, **361**, 1005
- Fossum, A., & Carlsson, M. 2005, *ApJ*, **625**, 556
- Hauchecorne, A., Meftah, M., Irbah, A., et al. 2014, *ApJ*, **783**, 127
- Kilcik, A., Sigismondi, C., Rozelot, J. P., & Guhl, K. 2009, *SoPh*, **257**, 237
- Kubo, Y. 1993, *PASJ*, **45**, 819
- Kuhn, J. R., Bush, R. I., Emilio, M., & Scherrer, P. H. 2004, *ApJ*, **613**, 1241
- Meftah, M., Corbard, T., Irbah, A., et al. 2014a, *A&A*, **569**, A60
- Meftah, M., Hauchecorne, A., Crepel, M., et al. 2014b, *SoPh*, **289**, 1
- Norton, A. A., Graham, J. P., Ulrich, R. K., et al. 2006, *SoPh*, **239**, 19
- Parkinson, J. H., Morrison, L. V., & Stephenson, F. R. 1980, *Natur*, **288**, 548
- Rozelot, J. P., & Damiani, C. 2012, *EPJH*, **37**, 709
- Sánchez, M., Parra, F., Soler, M., & Soto, R. 1995, *A&AS*, **110**, 351
- Shapiro, I. I. 1980, *Sci*, **208**, 51
- Sofia, S., Dunham, D. W., Dunham, J. B., & Fiala, A. D. 1983, *Natur*, **304**, 522
- Sofia, S., Girard, T. M., Sofia, U. J., et al. 2013, *MNRAS*, **436**, 3
- Thuillier, G., Sofia, S., & Haberleiter, M. 2005, *AdSpR*, **35**, 329
- Wachter, R., Schou, J., Rabello-Soares, M. C., et al. 2012, *SoPh*, **275**, 261
- Wittmann, A. D. 2003, *AN*, **324**, 378